Multipseudopotential interaction models for thermal lattice Boltzmann method simulations

Multipseudopotential interaction models for thermal lattice Boltzmann method simulations

Kamil Pasieczynski and Baixin Chen*
School of Engineering and Physical Sciences, Heriot-Watt University, Edinburgh EH14 4AS, United Kingdom

(Received 5 April 2020; accepted 6 July 2020; published 28 July 2020)

In this work, in the first instance, the multipseudopotential interaction (MPI) model's capabilities are extended for hydrodynamic simulations. This is achieved by combining MPI with the multiple-relaxation-time collision operator and with surface tension modification methods. A method of approaching thermodynamic consistency is also proposed, which consists of splitting the ε_j term into separate terms. One of these terms is used in the calculation of the interparticle force, and the second one is used in the forcing scheme. Secondly, MPI is combined with thermal models in order to simulate droplet evaporation and bubble nucleation in pool boiling. Thermal coupling is implemented using a double distribution function thermal model and a hybrid thermal model. It is found that MPI thermal models obey the D^2-law closely for droplet evaporation. MPI is also found to correctly simulate bubble nucleation and departure from the heating element during nucleate pool boiling. It can be suggested that MPI thermal models are comparatively better suited to thermal simulations at low reduced temperatures than single pseudopotential interaction models, although such cases remain very challenging. Droplet evaporation simulations are carried out at a reduced temperature (T_r) of 0.6 by setting the parameters in the Peng-Robinson equation of state to $a = 1/6272$ and $b = 1/168$.

DOI: 10.1103/PhysRevE.102.013311

I. INTRODUCTION

The lattice Boltzmann method (LBM) [1] is a rapidly evolving method for simulation of fluid dynamics. It shows promise for applications involving multiphase and thermal simulations. Numerical simulation methods are powerful tools for studying boiling phenomena due to the multiple thermophysical properties and other factors that influence heat-transfer processes [2]. On the other hand, difficulties in numerical studies of the boiling process emerge due to the multiple scales involved and phase interface movement [2]. These factors suggest that mesoscopic methods, such as the LBM, are promising tools for studying boiling phenomena. The purpose of this work is to develop the multipseudopotential interaction (MPI) [3,4] model into a simulation tool capable of investigation of thermal phenomena. MPI belongs to the pseudopotential family of multiphase LBM simulation tools originating in the Shan-Chen model [5,6].

A number of groups of thermal models for the lattice Boltzmann method exist in the literature. Thermal models for the lattice Boltzmann method can be divided into the following categories [7]: multispeed [8], double-distribution function (DDF) [9], and hybrid [10].

The DDF and hybrid thermal models are often used with pseudopotential and phase-field multiphase LBMs [7]. In DDF models, two distribution functions need to be solved. One set of calculations is performed to solve the hydrodynamic distribution function, and another is performed to solve the thermal distribution function. The thermal distribution functions are solved within the framework of the LBM. The DDF models can be further subdivided into internal-energy-based [11], total-energy-based [12], and temperature-based [9] models [7]. The hybrid [10,13] models work similarly to the DDF models in the sense that the solution of the hydrodynamic equations is performed separately from the solution of the thermal equations [7]. Unlike in the case of DDF models, hybrid methods solve the temperature equations using conventional numerical methods, i.e., the finite-volume or finite-difference methods [7]. In his book, Patankar outlined numerical discretization methods used in traditional computational fluid dynamics (CFD) codes [14]. As an example, the fourth-order Runge-Kutta method can be used to calculate temperature evolution [15].

Li *et al.* [16] used the Gong-Cheng [17] model to illustrate numerical errors in thermal simulations, including the failure to obey the D^2-law [18] for droplet evaporation. The D^2-law [18] states that the square of the droplet diameter should change linearly over time [16,18]. It is the simplest possible description of droplet vaporization and combustion, and it contains the following assumptions: spherical symmetry, no spray effects, diffusion being rate-controlling, isobaric process, flame-sheet combustion, constant gas-phase transport properties, and gas-phase quasisteadiness [18]. Later, Li *et al.* [19] pointed out inconsistencies in Gong *et al.*'s [20] derivation of the temperature equation.

Recently, a number of popular thermal models for the LBM were analyzed by Hu *et al.* [21] and ranked according to their qualities. One of the main observations was that the temperature-based models are superior to the internal-energy-based models in terms of accuracy and thermodynamic consistency [21]. The tested models were ranked from best to worst in the following order [21]: the hybrid finite-difference scheme by Li *et al.* [15]; the modified internal-energy-based model by Li *et al.* [16]; the temperature-based model by Hazi

*Author to whom all correspondence should be addressed: b.chen@hw.ac.uk

and Markus [22]; the simplified temperature-based model by Peng *et al.* [23]; and the internal-energy-based model by Zhang and Chen [24].

Hu *et al.* [21] also carried out simulations to investigate heat transition through a static phase interface by combining thermal models with the piecewise-linear equation of state (EOS) [25]. Combining the piecewise-linear EOS with thermal models allowed the authors to uncouple the effect of temperature on density and to prevent phase change. Simultaneously, Hu and Liu [26] developed the idea of using the piecewise-linear EOS for thermal modeling with phase change. The effects of temperature were replaced by the degree of superheat, due to the assumption that the degree of superheat has little influence on the liquid properties [26]. Phase change effects were introduced into the pressure calculations [26].

The subsequent sections of the paper are organized as follows: In Sec. II the MPI model is combined with the MRT collision operator, Sec. III introduces the thermal MRT-MPI model, Sec. IV presents the results of numerical simulations, and Sec. V concludes this work.

II. MRT-MPI MODEL

This section outlines the details of the MPI model combined with the MRT collision operator [27]. The combination of MPI with MRT allows the model to simulate more challenging cases than are achievable with the single-relaxation-time (SRT) Bhatnagar-Gross-Krook (BGK) [28] collision operator. Multiple pseudopotentials can be described using the following equations [4]:

$$\boldsymbol{F} = \boldsymbol{F}^{(1)} + \boldsymbol{F}^{(2)} + \ldots + \boldsymbol{F}^{(n)}, \tag{1}$$

$$\boldsymbol{F} = \sum_{j=1}^{n} -G_j(\boldsymbol{x})\psi_j(\boldsymbol{x})c_s^2 \sum_{\alpha=1}^{N} w(|\boldsymbol{e}_\alpha|^2)\psi_j(\boldsymbol{x}+\boldsymbol{e}_\alpha)\boldsymbol{e}_\alpha, \tag{2}$$

$$\psi_j(\rho) = \left(\frac{\rho}{\lambda_j\varepsilon_j + C_j\rho}\right)^{1/\varepsilon_j}. \tag{3}$$

Equation (2) is suitable for isothermal cases. In this work, the following intermolecular force expression is proposed for thermal phenomena:

$$\boldsymbol{F}^{\mathrm{MPI}} = \sum_{j=1}^{n} -\sqrt{|G_j(\boldsymbol{x})|}G_{\mathrm{sign},j}\psi_j(\boldsymbol{x})c_s^2 \times \sum_{\alpha=1}^{N} w(|\boldsymbol{e}_\alpha|^2)\sqrt{|G_j(\boldsymbol{x}+\boldsymbol{e}_\alpha)|}\psi_j(\boldsymbol{x}+\boldsymbol{e}_\alpha)\boldsymbol{e}_\alpha. \tag{4}$$

A. Achievement of thermodynamic consistency

Thermodynamic inconsistency is a prominent shortcoming of pseudopotential models. The MPI-obtained coexistence densities at low reduced temperatures deviate from the thermodynamically consistent values. This behavior is observed for both the SRT and MRT collision operators. The deviation becomes significant at high density ratios, and this can be seen in Fig. 1.

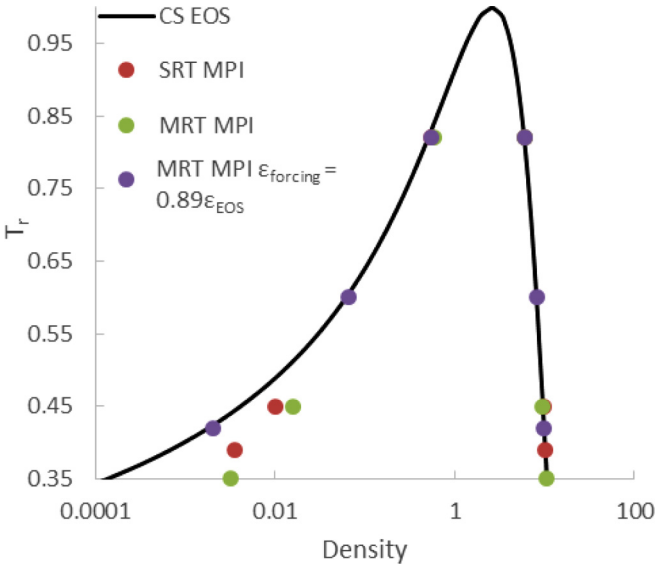

FIG. 1. Deviation of MPI from the thermodynamic coexistence densities when the SRT and MRT collision operators are used and the performance of the modification for a broad temperature range.

Thermodynamic consistency can be approached by splitting the epsilon into two separate values, i.e., one for use in the EOS and a second one for use in the forcing scheme. Thus, the multipseudopotential changes its form from

$$\psi_j = \left(\frac{\rho}{\lambda_j\varepsilon_j + C_j\rho}\right)^{1/\varepsilon_j} \tag{5}$$

to the following expression:

$$\psi_j = \left(\frac{\rho}{\lambda_j\varepsilon_{\mathrm{EOS},j} + C_j\rho}\right)^{1/\varepsilon_{\mathrm{EOS},j}}. \tag{6}$$

This modification allows the user to set the ε to a different value in the forcing scheme than in the pseudopotential calculation in order to adjust the density ratio without affecting the equation of state introduced by the MPI model. Introduction of unnecessary modifications to the equation of state is not desired. For example, good results were obtained by setting the value of $\varepsilon_{\mathrm{Forcing},j}$ to 0.89 times the value of $\varepsilon_{\mathrm{EOS},j}$: $\varepsilon_{\mathrm{Forcing},j} = 0.89\varepsilon_{\mathrm{EOS},j}$.

The Li-Luo method [29] for achievement of thermodynamic consistency for the MRT collision operator can then be modified to the following for use with MPI:

$$6(u_xF_x + u_yF_y) + \sum_j \frac{12\frac{\varepsilon_{\mathrm{Forcing},j}}{-16G_j}|\boldsymbol{F}_j|^2}{{\psi_j}^2\Delta t(\tau_e - 0.5)}. \tag{7}$$

Figure 1 above shows that the MPI modification splitting ε into two separate values allows to approach thermodynamic consistency closely across the entire range of reduced temperature.

B. Spurious velocities

Spurious velocities are investigated in this subsection. Both Yuan-Schaefer [30] (a popular single pseudopotential

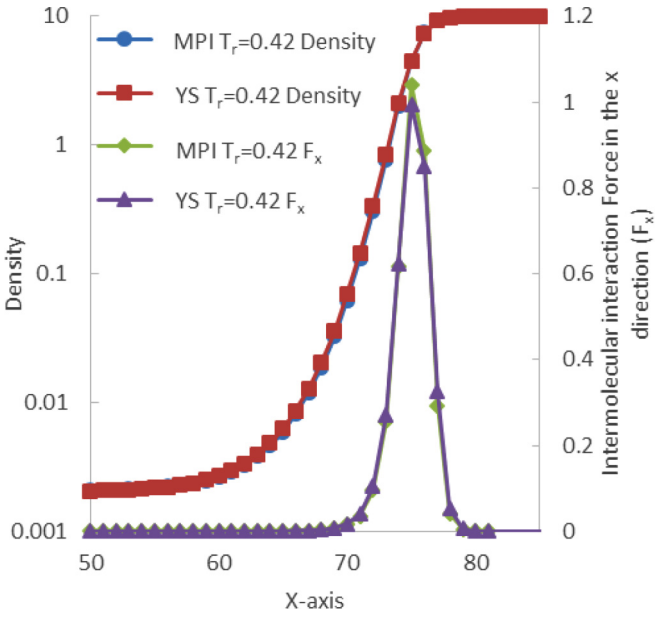

FIG. 2. Interparticle force generated by MPI and YS methods at the same density ratio. Carnahan-Starling a parameter was set to 0.01, b was set to 0.2, and R was set to 1. The value of $\varepsilon_{\text{Forcing},j}$ in MPI was set to $0.89\varepsilon_{\text{EOS},j}$ and the values of k_1 and k_2 in the Huang-Wu forcing scheme for the SPI model were set to 0.0 and -0.2188, respectively.

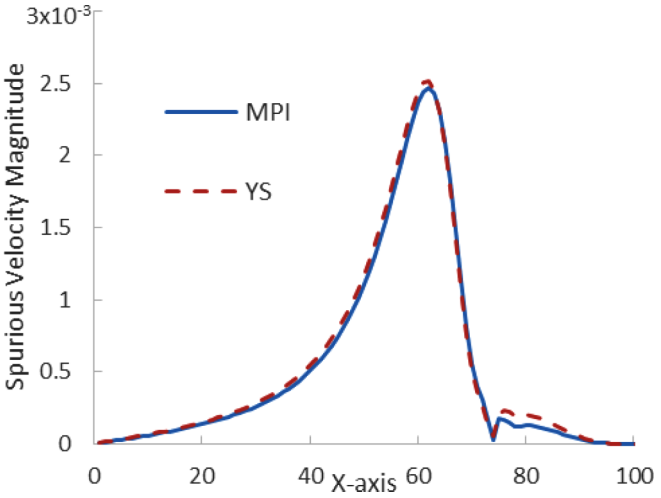

FIG. 3. Spurious velocity magnitude generated by the MPI and YS methods at $T_r = 0.42$ ($\tau_v = 1$ and $\Lambda = 1/12$).

interaction method of including cubic equations of state) and MPI [3,4] models give practically the same spurious velocities when corresponding values of EOS parameters are used in both models. This is caused by the fact that both models generate almost identical intermolecular interaction force. A comparison of the intermolecular forces generated by both methods at the same conditions is presented in Fig. 2. The results were obtained by setting Carnahan-Starling a to 0.01, b to 0.2, and R to 1 for both methods. MPI was implemented using the adapted Li-Luo forcing method, given by Eq. (7), with $\varepsilon_{\text{Forcing},j} = 0.89\varepsilon_{\text{EOS},j}$ as discussed in the previous subsection. The YS method was implemented using the Huang-Wu method with k_1 set to 0.0 and k_2 set to -0.2188. The resultant spurious velocity magnitude for the MPI and YS simulations depicted in Fig. 2 is presented in Fig. 3.

III. HYDRODYNAMIC MRT-MPI COMBINED WITH THERMAL LBM MODELS

In this section, the MRT-MPI model is combined with two thermal models in order to extend its capability to the study of thermal effects. Based on the recommendations of Hu *et al.* [21] and Li *et al.* [16], the models used in this work belong to the DDF and hybrid thermal LBM categories. The equations that need to be solved in the fourth-order Runge-Kutta scheme used in the hybrid thermal LBM model [15] are listed below:

$$T^{t+\delta t} = T^t + \frac{\delta_t}{6}(h_1 + 2h_2 + 2h_3 + h_4), \tag{8}$$

$$h_1 = K(T^t), \tag{9}$$

$$h_2 = K\left(T^t + \frac{\delta_t}{2}h_1\right), \tag{10}$$

$$h_3 = K\left(T^t + \frac{\delta_t}{2}h_2\right), \tag{11}$$

$$h_4 = K(T^t + \delta_t h_3). \tag{12}$$

The Runge-Kutta method is an iterative method for temporal discretization. The form of the function K with temperature as the argument or independent variable depends on the temperature equation to be solved. The equation that needs to be solved for Li *et al.*'s [15] hybrid thermal model is the following:

$$K(T^t) = -\boldsymbol{u}\cdot\nabla T + \frac{\lambda}{\rho c_V}\nabla\cdot(\lambda\nabla T) - \frac{T}{\rho c_V}\left(\frac{\partial p_{\text{EOS}}}{\partial T}\right)_\rho \nabla\cdot\boldsymbol{u}. \tag{13}$$

The equations constituting the DDF model by Li *et al.* [16] take the following forms:

$$g_\alpha(\boldsymbol{x} + \boldsymbol{e}_\alpha\delta_t, t + \delta_t) = g^*_\alpha(\boldsymbol{x}, t), \tag{14}$$

$$\boldsymbol{g}^* = \boldsymbol{M}^{-1}\boldsymbol{m}^*, \tag{15}$$

$$\boldsymbol{m}^* = \boldsymbol{m} - \boldsymbol{\Lambda}(\boldsymbol{m} - \boldsymbol{m}^{\text{eq}}) + \delta_t\boldsymbol{S}. \tag{16}$$

The thermal model is implemented using the MRT collision operator with [16]

$$\boldsymbol{\Lambda} = \text{diag}(s_0, s_1, s_2, s_3, s_4, s_5, s_6, s_7, s_8), \tag{17}$$

$$\boldsymbol{m}^{\text{eq}} = T(1, -2, 2, u_x, -u_x, u_y, -u_y, 0, 0)^T, \tag{18}$$

$$\boldsymbol{S} = (S_0, 0, 0, 0, 0, 0, 0, 0, 0)^T, \tag{19}$$

$$S_0 = \phi + 0.5\delta_t\partial_t\phi, \tag{20}$$

where

$$\phi = \frac{1}{\rho c_V}\nabla\cdot(\lambda\nabla T) - \nabla\cdot(k\nabla T) + T\left[1 - \frac{1}{\rho c_V}\left(\frac{\partial p_{\mathrm{EOS}}}{\partial T}\right)_\rho\right]\nabla\cdot\boldsymbol{u}, \tag{21}$$

$$k = \eta c_s^2 \delta_t, \tag{22}$$

$$\eta = \left(\frac{1}{s_3} - \frac{1}{2}\right) = \left(\frac{1}{s_5} - \frac{1}{2}\right). \tag{23}$$

In addition, the third and fourth temperature distribution functions in the moment space are modified in order to remove the $\partial_{t0}(T\mathbf{u})$ error according to [16]

$$m^*_{3,\mathrm{New}} = m^*_3 + \delta_t\left(1 - \frac{s_3}{2}\right)s_4\left(m_4 - m_4^{\mathrm{eq}}\right), \tag{24}$$

$$m^*_{5,\mathrm{New}} = m^*_5 + \delta_t\left(1 - \frac{s_5}{2}\right)s_6\left(m_6 - m_6^{\mathrm{eq}}\right). \tag{25}$$

The partial derivative responsible for phase-change was taken to be the following for the Peng-Robinson and Carnahan-Starling equations of state, respectively:

$$\left(\frac{\partial p_{\mathrm{PR}}}{\partial T}\right)_\rho = \frac{\rho R}{1 - b\rho}, \tag{26}$$

$$\left(\frac{\partial p_{\mathrm{CS}}}{\partial T}\right)_\rho = \rho R\frac{1 + \frac{b\rho}{4} + \left(\frac{b\rho}{4}\right)^2 - \left(\frac{b\rho}{4}\right)^3}{\left(1 - \frac{b\rho}{4}\right)^3}. \tag{27}$$

Gradient terms were calculated using the second-order isotropic difference scheme [7]:

$$\partial_i T(\boldsymbol{x}) \approx \frac{1}{c_s^2\delta_t}\sum_\alpha \omega_\alpha T(\boldsymbol{x} + \boldsymbol{e}_\alpha\delta_t)e_{\alpha i}. \tag{28}$$

Laplacian terms were calculated using the second-order isotropic difference scheme [7,31] and using the isotropic discrete Laplacian operators [32]. The second-order isotropic difference scheme takes the following form [7]:

$$\nabla^2 T(x) \approx \frac{2}{c_s^2\delta_t^2}\sum_\alpha \omega_\alpha[T(\boldsymbol{x} + \boldsymbol{e}_\alpha\delta_t) - T(\boldsymbol{x})]. \tag{29}$$

The isotropic discrete Laplacian operator takes the following form [32]:

$$L(\boldsymbol{x})_{\mathrm{D2Q9}} \equiv \nabla^2 T(x) = \frac{1}{6}\left[4\sum_{i=1}^{4} T_i^{(1)} + \sum_{i=1}^{4} T_i^{(2)} - 20T^{(0)}\right]. \tag{30}$$

Both of the above methods for calculating the Laplacian of temperature provided the same results as illustrated in Fig. 4

However, for the sake of consistency, the second-order isotropic difference scheme was used exclusively to obtain the data discussed in this paper.

The simplest way of including thermal effects in the MPI model is to combine the hydrodynamic model with one of the thermal models and to make the temperature terms in MPI location-dependent with temperature updated by the implemented thermal model. In isothermal models, the temperature

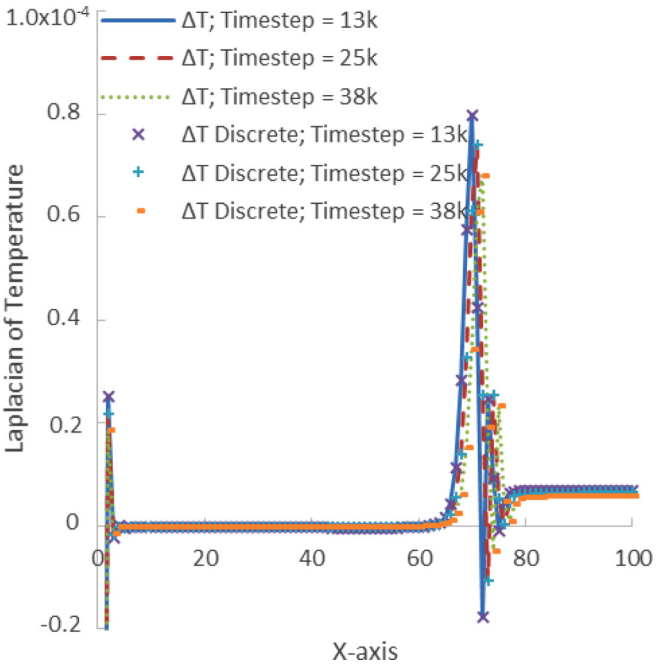

FIG. 4. Spatial distribution of the Laplacian operator of temperature calculated using the second-order isotropic difference scheme and the isotropic discrete scheme for the case of droplet evaporation at time steps equal to 13 000, 25 000, and 38 000.

term is constant throughout the computational domain and it is prescribed for the entire simulation duration during initialization. The intermolecular force in multipseudopotential interaction models is calculated according to

$$\boldsymbol{F} = \sum_{j=1}^{n} -G_j(\boldsymbol{x})\psi_j(\boldsymbol{x})c_s^2\sum_{\alpha=1}^{N} w(|\boldsymbol{e}_\alpha|^2)\psi_j(\boldsymbol{x} + \boldsymbol{e}_\alpha)\boldsymbol{e}_\alpha. \tag{31}$$

It is clear that the ψ_j term does not contain temperature-related parameters as evident in Eqs. (5) and (6). Please refer to Ref. [4] for details of the MPI parameters for a number of cubic equations of state. Temperature in MPI models is contained in the G terms. Hence, thermal MPI implemented in this way incorporates thermal effects only at the local site $\boldsymbol{x}$ in the calculation of the intermolecular force $\boldsymbol{F}$. This formulation of the intermolecular force is suitable for isothermal cases, where the temperature is constant throughout the computational domain.

In reality, intermolecular forces reflect the effect of temperatures of the interacting particles. This effect is naturally present in thermal models using the square-root form of the pseudopotential including the thermal YS models. In these models, temperature effects are equally weighted at $\boldsymbol{x}$ and $\boldsymbol{x} + \boldsymbol{e}_\alpha$. Temperature-containing terms in pseudopotential models employing the square-root form of ψ are highlighted in the following equation:

$$\boldsymbol{F} = -G\psi(\boldsymbol{x})c_s^2\sum_{\alpha=1}^{N} w(|\boldsymbol{e}_\alpha|^2)\psi(\boldsymbol{x} + \boldsymbol{e}_\alpha)\boldsymbol{e}_\alpha. \tag{32}$$

Unmodified thermal MPI without temperature being included at $\boldsymbol{x} + \boldsymbol{e}_\alpha$ sites can simulate droplet evaporation, but

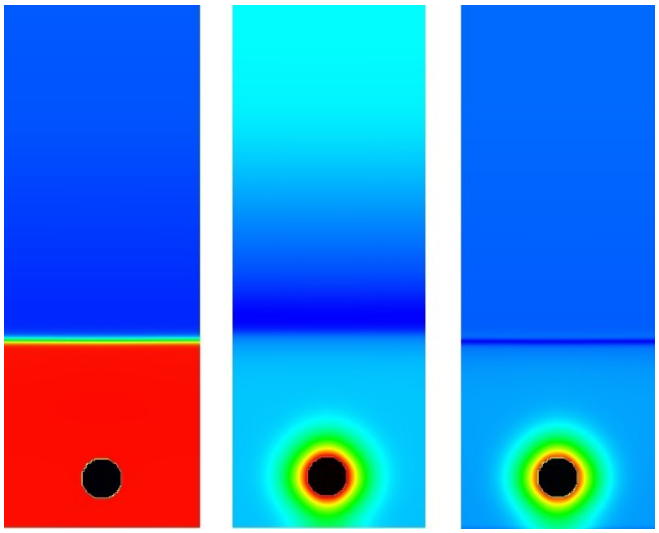

FIG. 5. Density field on the left-hand side, temperature field in the middle, and pressure field on the right-hand side to illustrate the results of unmodified thermal MPI in bubble nucleation simulations. The black tube in the liquid phase is used as the heating element.

it cannot simulate bubble nucleation during pool boiling. Instead of vapor being generated, a high-pressure zone is created adjacent to the heating element without phase change occurring, as illustrated in Fig. 5. Eventually, the accumulation of energy in the liquid without phase change leads to generation of turbulence at the liquid-vapor interface.

To accurately incorporate thermal effects, the thermal MPI model needs to be modified. The intermolecular force can be rewritten in the following manner in order to allow inclusion of thermal effects at $\boldsymbol{x}$ and $\boldsymbol{x}+\boldsymbol{e}_\alpha$:

$$\boldsymbol{F} = \sum_{j=1}^{n} -\sqrt{|G_j(\boldsymbol{x})|}G_{\mathrm{sign},j}\psi_j(\boldsymbol{x})c_s^2 \times \sum_{\alpha=1}^{N} w(|\boldsymbol{e}_\alpha|^2)\sqrt{|G_j(\boldsymbol{x}+\boldsymbol{e}_\alpha)|}\psi_j(\boldsymbol{x}+\boldsymbol{e}_\alpha)\boldsymbol{e}_\alpha. \quad (33)$$

A second G term is introduced to allow incorporation of thermal effects at $\boldsymbol{x}+\boldsymbol{e}_\alpha$ sites. To take account of the fact that a second G term has been introduced, it is necessary to take the square root of the G terms. This treatment of the G terms means that both terms are equally weighted in the calculation of the intermolecular forces. A sign function is also necessary in order to take the negative signs outside of the square-root terms to prevent generation of complex numbers. Absolute values of the G terms are used in the square roots.

IV. NUMERICAL SIMULATIONS

This section provides the results of numerical simulations carried out using the thermal models discussed in this paper. The thermal MPI model implemented in the way detailed in Sec. III can correctly simulate droplet evaporation and bubble nucleation during pool boiling.

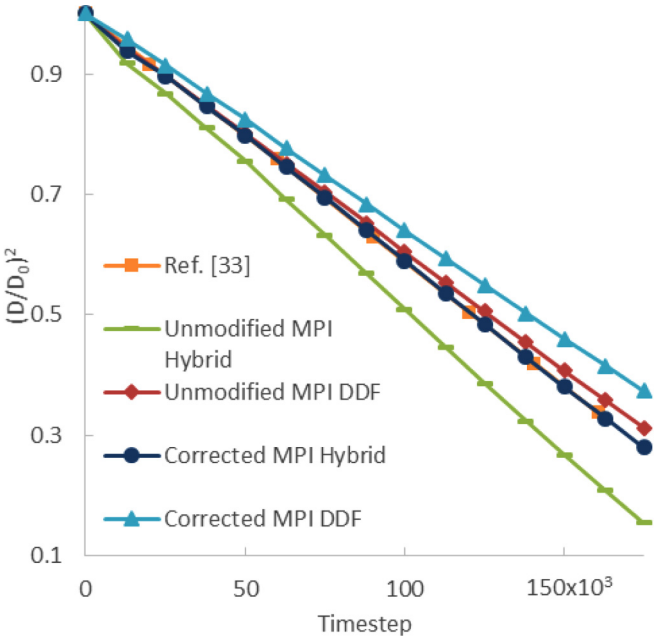

FIG. 6. Verification of the D^2-law during droplet evaporation for the unmodified and corrected thermal MPI. The initial droplet diameter (D_0) was 60 lattice units. Reduced temperature was set to 0.86 and the superheat with respect to the saturation temperature was set to 0.14 times the critical temperature. Thermal conductivity was set to 2/3 and heat capacity at constant volume was set to 5. Acentric factor was set to 0.344, PR EOS a to 3/49, b to 2/21. Comparison to data in Ref. [33].

A. Droplet evaporation

The ability to correctly simulate droplet evaporation is a basic requirement of thermal simulation tools. Figure 6 illustrates the fact that thermal MPI correctly simulates droplet evaporation. Droplet evaporation can be tested using the D^2-law [18]. To validate conformity to the D^2-law [18], simulations were carried out in a 200×200 gravity-free domain with periodic boundary conditions at all four sides. The vapor surrounding the liquid droplet was initialized at a superheated temperature that was higher than the saturation temperature of the liquid by 0.14 times the critical temperature (i.e., by $0.14T_c$). The superheat was enforced at the periodic boundaries during the simulation. Heat capacity at constant volume (c_V) was equal to 5. The value of thermal conductivity (λ) was constant in the computational domain at 2/3, leading to the following simplification in the temperature equations: $\nabla \cdot (\lambda \nabla T) = \lambda \nabla^2 T$.

Bulk viscosity was set to be equal to kinematic viscosity. The magic parameter was set to 1/12 in the hydrodynamic MRT collision operator. All of the relaxation rates in the thermal diagonal matrix ($\boldsymbol{\Lambda}$) were set to 1.0, resulting in the k parameter in the temperature equation being equal to 1/6. In the double distribution function (DDF) model of Li *et al.*, k is simply a constant without physical meaning [16]. The simulations using both MPI and YS methods were carried out at a reduced temperature of 0.86 with the acentric factor equal to 0.344, and the Peng-Robinson equation of state $a = 3/49$, $b = 2/21$, and $R = 1$. MPI was implemented using the

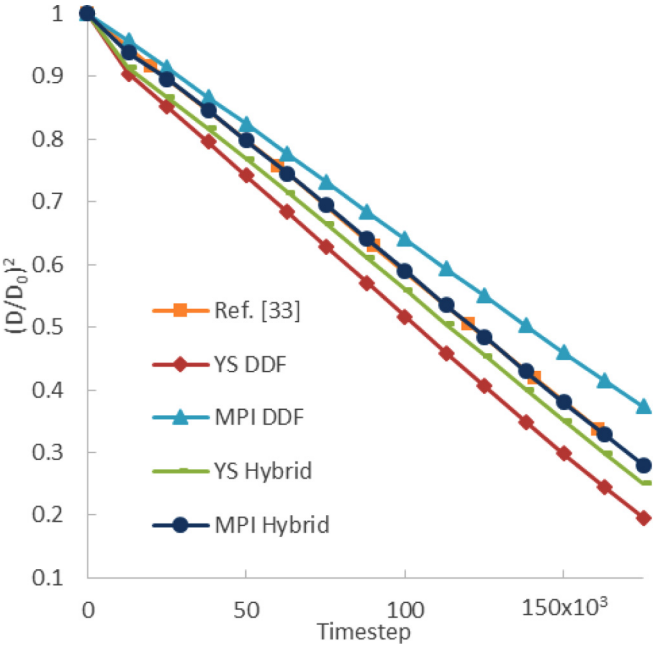

FIG. 7. Comparison of droplet evaporation rates of YS and MPI thermal models. Reference [33] data plotted for validation purposes. The initial droplet diameter (D_0) was 60 lattice units. $T_r = 0.86$, initial droplet diameter = 60, superheat = $0.14T_c$, $c_v = 5$, thermal conductivity = 2/3, acentric factor = 0.344, PR $a = 3/49$, and PR $b = 2/21$.

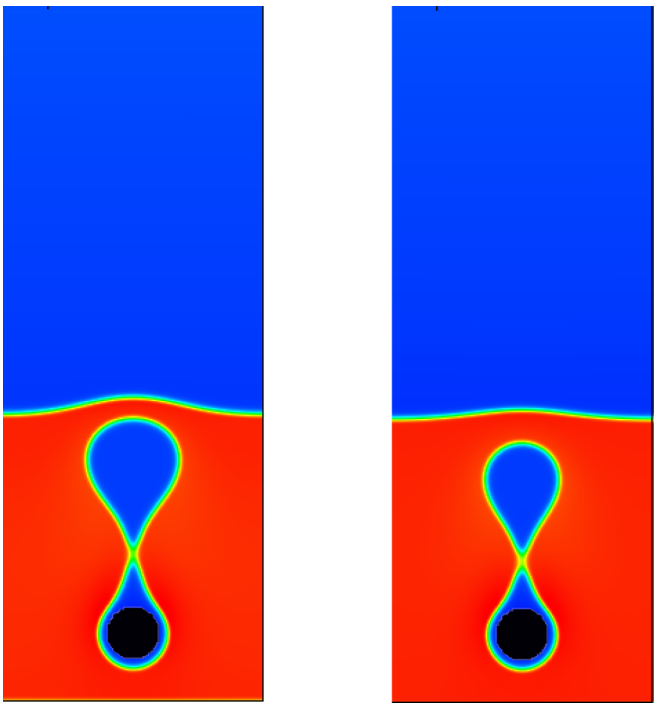

FIG. 8. Comparison of bubble nucleation and departure from a heating element. The image on the left-hand side was obtained using the YS DDF model, and the image on the right-hand side was obtained using the MPI DDF model.

adapted Li-Luo forcing method with $\varepsilon_{\text{Forcing},j}$ set to 0.89 times the value of $\varepsilon_{\text{EOS},j}$. The YS method was implemented using the Huang-Wu forcing method with k_1 set to 0.0 and k_2 set to -0.2188.

Figure 7 compares droplet evaporation rates obtained using the YS and MPI thermal models. The rate of evaporation obtained using the MPI hybrid model is the same as the rate of evaporation for a fourth-order Runge-Kutta hybrid model detailed in Ref. [33]. The simulation parameters were chosen to be the same as those in Ref. [33]. MPI thermal models provide straight lines in simulations of droplet evaporation that fulfill the D^2-law. Therefore, it can be stated that MPI is comparatively well suited to thermal simulations. In comparison, YS thermal models provide lines that are slightly less straight, with a steeper drop in droplet diameter in the first 13 000 time steps. The rates of evaporation obtained using the MPI models are lower than those obtained using the YS models.

B. Bubble nucleation

Figure 8 illustrates that both YS DDF and MPI DDF models can simulate bubble nucleation and departure from a heating element. The black circle submerged in the liquid phase is meant to represent a heating element, which could be a tube in a heat exchanger supplying heat to the liquid phase. Thus, simulation of complex heat exchanger geometries is possible using the models. The domain size was 150 nodes in the x direction by 400 nodes in the y direction. Top and bottom boundaries were set to bounce back, and the left- and right-hand-side boundaries were periodic. Liquid was located in the bottom of the computational domain up to a thickness of 150 lattice units with the space above it filled with vapor. The diameter of the heating element was set to 30 lattice units, and its center was located 40 lattice units above the bottom boundary in the middle of the x-axis. Heat was supplied to the liquid phase along the entire length of the circumference of the heating element. The temperature of the heating element was set to 1.25 times the critical temperature ($1.25T_c$). Heat capacity at constant volume (c_v) was set to 5.0, and kinematic viscosity was set to 0.1 ($\tau_v = 0.8$). The value of gravity was set to -2.5×10^{-5} in the y direction, and the gravity force was implemented using the difference between the local density and the average density within the fluid domain: $F_{\text{gravity},y} = -2.5 \times 10^{-5}(\rho - \rho_{\text{average}})$.

This method of introducing gravity prevents injection of net momentum into the simulation domain [34]. In the hydrodynamic relaxation matrix, the value of bulk viscosity was set to the same value as the kinematic viscosity. The hydrodynamic MRT magic parameter was set to 1/12. All of the relaxation rates in the thermal diagonal matrix ($\mathbf{\Lambda}$) were set to 1.0. Hence, k in the temperature equation was equal to 1/6. Thermal diffusivity (χ) was set to 0.06. This value of thermal diffusivity was used in the calculation of thermal conductivity. Thermal conductivity (λ) was set to be variable, and it was obtained from the following equation: $\lambda = \rho c_V \chi$.

Opting for a location-dependent value of thermal conductivity necessitates the following treatment of $\nabla \cdot (\lambda \nabla T)$ in the temperature equation $\nabla \cdot (\lambda \nabla T) = \lambda \nabla^2 T + \nabla \lambda \cdot \nabla T$.

A cubic equation of state was employed in the simulations. The chosen equation of state was the Peng-Robinson EOS,

TABLE I. Investigation of the effects of changing the G weightings on bubble nucleation.

χ	Relative weighting and observations
2	(100% and 0%) original thermal MPI—no nucleation and generation of turbulence at liquid-vapor interface
1.5	(75% and 25%) no nucleation—generation of two-phase mixture
1.1	(55% and 45%) bubble nucleation no departure
1	Equal weighting—correct bubble nucleation
0.9	(45% and 55%) bubble nucleation
0.75	(37.5% and 62.5%) unstable after 100 time steps
0.5	(25% and 75%) unstable
0	(0% and 100%) immediately unstable

because it offers good stability [30] and is widely used in the literature, allowing comparison to published results. The models are compared at a reduced temperature of 0.86 with parameters in the Peng-Robinson equation of state set to $a = 3/49$, $b = 2/21$, $R = 1$, and the acentric parameter equal to 0.344 (the acentric parameter value for water). MPI was implemented using the adapted Li-Luo forcing method with $\varepsilon_{\text{Forcing},j}$ set to 0.89 times the value of $\varepsilon_{\text{EOS},j}$. The YS method was implemented using the Huang-Wu forcing method with k_1 set to 0.0 and k_2 set to -0.2188. Neither forcing scheme is set to modify surface tension, which means that both MPI and YS methods generate the same surface tension values, equal to 0.0701, in this case. Both models generate a bubble that departs the heating element at the 9700 time step. As mentioned above, MPI results in a lower rate of evaporation than the YS model. Hence, the bubble generated by the MPI model is slightly smaller than the bubble generated by the YS model.

C. Modification of the G weightings

The intermolecular force expression in the thermal MPI model can be modified to allow different weightings of $G_j(\boldsymbol{x})$ and $G_j(\boldsymbol{x}+\boldsymbol{e}_\alpha)$. The weightings can be modified by setting powers of the G terms to the following:

$$\boldsymbol{F} = \sum_{j=1}^{n} -|G_j(\boldsymbol{x})|^{\frac{\chi}{2}} G_{\text{sign},j}\psi_j(\boldsymbol{x})c_s^2 \times \sum_{\alpha=1}^{N} w(|\boldsymbol{e}_\alpha|^2)|G_j(\boldsymbol{x}+\boldsymbol{e}_\alpha)|^{\frac{2-\chi}{2}}\psi_j(\boldsymbol{x}+\boldsymbol{e}_\alpha)\boldsymbol{e}_\alpha. \quad (34)$$

Lower-case Greek letter chi (χ) was introduced into the above expression to allow modification of the G weightings. Table I lists the effects of changing the G weightings on bubble nucleation. Based on the findings, equal weighting of the G terms in thermal MPI is the appropriate choice. This weighting coincides with the treatment of thermal effects in thermal YS models.

D. Surface tension adjustment in thermal MPI

Thermal MPI can be combined with either the Li-Luo method [35] or the Huang-Wu method [36] for surface tension modification. In this subsection, the effects of decreasing and increasing surface tension are examined in bubble nucleation simulations using the thermal MPI DDF model. The Li-Luo [35] method has to be adapted for use with the MPI model into the following expression:

$$\boldsymbol{Q} = \sum_{j=1}^{n} \kappa \frac{G_j(\boldsymbol{x})}{2}\psi_j(\boldsymbol{x}) \times \sum_{\alpha=1}^{8} w(|\boldsymbol{e}_\alpha|^2)[\psi_j(\boldsymbol{x}+\boldsymbol{e}_\alpha)-\psi_j(\boldsymbol{x})]\boldsymbol{e}_\alpha\boldsymbol{e}_\alpha, \quad (35)$$

and the Huang-Wu [36] method should take the following form in order to allow surface tension modification in MPI models:

$$\boldsymbol{Q_m} = \begin{bmatrix} 0 \\ 3\sum_{j=1}^{n}\left(k_1 + 2\left(\frac{\varepsilon_j}{-8}-k_1\right)\right)\frac{|\boldsymbol{F}_j|^2}{G_j{\psi_j}^2} \\ -3\sum_{j=1}^{n}\left(k_1 + 2\left(\frac{\varepsilon_j}{-8}-k_1\right)\right)\frac{|\boldsymbol{F}_j|^2}{G_j{\psi_j}^2} \\ 0 \\ 0 \\ 0 \\ 0 \\ k_1\sum_{j=1}^{n}\frac{F_{x,j}^2-F_{y,j}^2}{G_j{\psi_j}^2} \\ k_1\sum_{j=1}^{n}\frac{F_{x,j}F_{y,j}}{G_j{\psi_j}^2} \end{bmatrix}. \quad (36)$$

The Li-Luo [35] method is better for reducing surface tension, and the Huang-Wu [36] method is more suitable for increasing surface tension. Consequently, the Li-Luo method was employed to reduce surface tension, and the Huang-Wu method was used to increase surface tension. Simulations were carried out using the same parameters as those described in Sec. IV B. Figure 9 illustrates bubble departure from the heating element as surface tension is reduced from the unmodified value of surface tension, i.e., from surface tension coefficient = 1.0.

Surface tension was reduced using the κ (kappa) parameter in the MPI-adapted Li-Luo method [35]. For example, in order to set the surface tension coefficient to 0.1, κ was set to

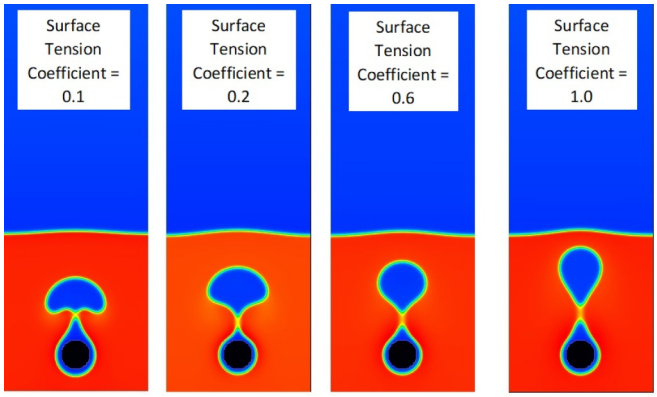

FIG. 9. Effect of reducing surface tension on the departure of a nucleated bubble from the heating element. Surface tension decreases from the right-hand side coefficient value of 1.0, through 0.6 and 0.2, down to 0.1 on the left-hand side.

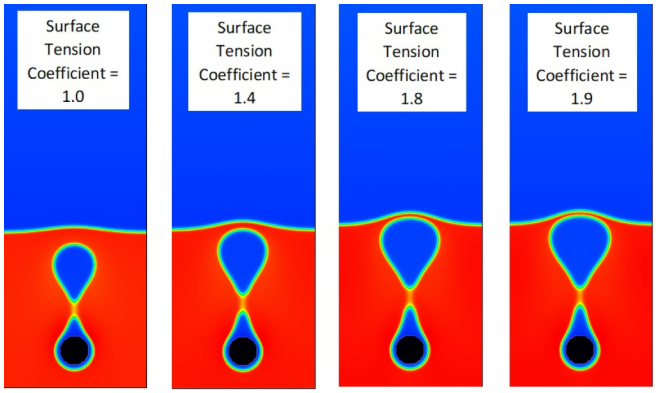

FIG. 10. Effect of increasing surface tension on the departure of a nucleated bubble. Surface tension coefficient increases from 1.0 on the left-hand side, though 1.4 and 1.8, up to 1.9 on the right-hand side.

0.9. Surface tension coefficient equal to 0.1 results in surface tension that is 10 times lower than the unmodified surface tension. Clearly, as surface tension is reduced, the shape of the bubble changes from a teardrop shape to a domelike shape. According to Fig. 10, higher values of surface tension require generation of larger bubbles in order for departure from the heating element to take place.

Surface tension was increased using the MPI-adapted Huang-Wu method. k_1 was adjusted to increase surface tension according to surface tension coefficient $= 1–6k_1$, while ε was kept constant by adjusting k_2 as required. An observation can be made that the higher the value of surface tension, the longer it takes for the bubble to depart the heating element. The amount of time steps taken to departure versus the surface tension coefficient is plotted in Fig. 11. The trend exhibits an observable departure from linearity. Detailed parameters at bubble departure are listed in Table II.

Surface tension was calculated using the usual method of measuring the pressure difference inside and outside of liquid droplets of varying diameters and applying Laplace's law to obtain surface tension. In this method, surface tension is the slope of a line with 1/radius on the x-axis and pressure difference on the y-axis. The values of bubble diameter, velocity, and density were calculated across the widest point of the departing bubble. They were used to calculate the Weber number (We) for the departing bubbles.

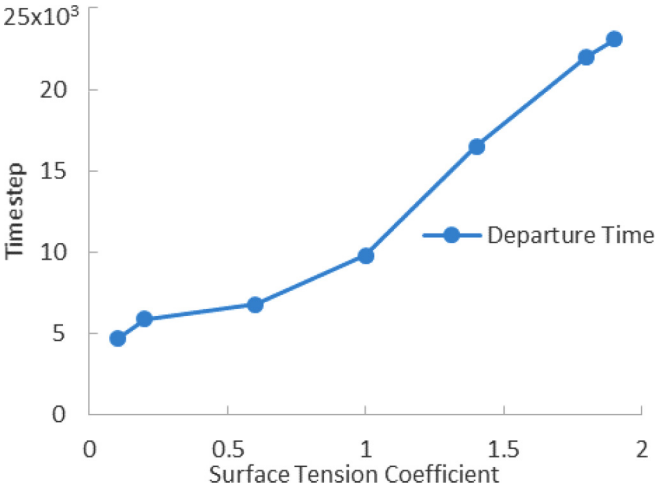

FIG. 11. Amount of time steps taken for the nucleated bubble to break free from the heating element at different values of surface tension.

The Weber number can be expressed as follows [37]:

$$\mathrm{We} = \frac{\rho u^2 d}{\sigma}. \tag{37}$$

It relates the inertial forces to the surface tension generated forces [37,38]. The Weber number is commonly used in the study of droplet and bubble breakup. For example, Unnikrishnan *et al.* [39] studied droplet splashing on chemically modified metallic surfaces at high Weber numbers (greater than 200). Montessori *et al.* [40] used the entropic LBM model to simulate droplet collisions at high Weber numbers. Different Weber number expressions also exist for use in various correlations, which are used in, for example, entrainment studies [41]. At very high values of the Weber number, surface tension considerations can be neglected [38]. We $= 1$ means that inertial and surface tension forces are equally important. The Weber number can also be used to predict the degree of surface turbulence, with a Weber number less than 2.0 indicting a lack of surface turbulence [42]. At very high values of the Weber number, the concept of surface turbulence becomes obsolete as the flow becomes jetting, spraying, or atomizing in nature [42]. According to Campbell, the Weber number has not been used to its full potential in some fields of research, including casting research [42].

The trend of Weber number versus surface tension coefficient is plotted in Fig. 12. Higher values of surface tension result in lower values of the Weber number of the departing bubble. Around We ≈ 2, bubble deformation from a teardrop shape is obvious and resembles a dome rather than a teardrop. At this stage, bubble shape becomes significantly more deformable during its buoyancy-driven ascent to the surface than at lower Weber numbers.

E. Achievement of lower reduced temperatures

In this subsection, the methods of achieving lower reduced temperatures are investigated using the pseudopotential thermal models. First, a method of carrying out thermal simulations using the piecewise-linear EOS is described. Secondly, the stable envelopes of reduced temperatures are presented.

1. Thermal piecewise-linear EOS model

A method of carrying out thermal simulations using the piecewise-linear EOS is presented here. It is clear that there are no temperature terms in the original piecewise-linear EOS [25]:

$$p_{\mathrm{EOS}} = \begin{cases} \rho\theta_V & \text{if } \rho \leqslant \rho_1, \\ \rho_1\theta_V + (\rho - \rho_1)\theta_M & \text{if } \rho_1 < \rho \leqslant \rho_2, \\ \rho_1\theta_V + (\rho_2 - \rho_1)\theta_M + (\rho - \rho_2)\theta_L & \text{if } \rho > \rho_2. \end{cases} \tag{38}$$

TABLE II. Data at bubble departure used to calculate the Weber number (We).

Surface tension coefficient	Surface tension	Departure time	Departure diameter	Velocity	Density	We
0.1	0.00701	4700	60.54	0.0207	0.4817	1.7833
0.2	0.01402	5900	60.93	0.0079	0.5017	0.136
0.6	0.04206	6800	48.73	0.017	0.5369	0.179
1	0.0701	9800	42.81	0.0144	0.5708	0.0724
1.4	0.09814	16500	49.61	0.0107	0.5162	0.0299
1.8	0.12618	22000	59.6	0.0089	0.5142	0.0192
1.9	0.13319	23100	61.65	0.0087	0.5135	0.0178

Temperature was introduced into the model by making the spinodal points temperature-dependent:

$$p_{\mathrm{EOS}} = \begin{cases} \rho\theta_V, & \text{if } \rho \leqslant \rho_1(T), \\ \rho_1(T)\theta_V + (\rho - \rho_1(T))\theta_M, & \text{if } \rho_1(T) < \rho \leqslant \rho_2(T), \\ \rho_1(T)\theta_V + (\rho_2(T) - \rho_1(T))\theta_M + (\rho - \rho_2(T))\theta_L & \text{if } \rho > \rho_2(T). \end{cases} \tag{39}$$

The spinodal points were calculated at a number of reduced temperatures for the Peng-Robinson EOS with the piecewise-linear EOS prescribing pressure slopes in each phase. The parameters were chosen in order to allow comparison with the YS and MPI thermal models which use the Peng-Robinson EOS directly. The spinodal points obtained are listed in Table III.

The spinodal points were plotted, and polynomial equations were used to estimate the trends in a number of sections of the reduced temperature range. The polynomial equations were then used in the thermal model to calculate the spinodal points at temperatures within the temperature range under investigation:

$$\rho_1(T_r = 1.0 - 0.9) = 19849T^2 - 3935.9T + 195.7, \tag{40}$$

$$\rho_1(T_r = 0.9 - 0.8) = 1571.4T^2 - 256.91T + 10.652, \tag{41}$$

$$\rho_1(T_r = 0.8 - 0.6) = 10138T^3 - 1921.1T^2 + 123.48T - 2.6842, \tag{42}$$

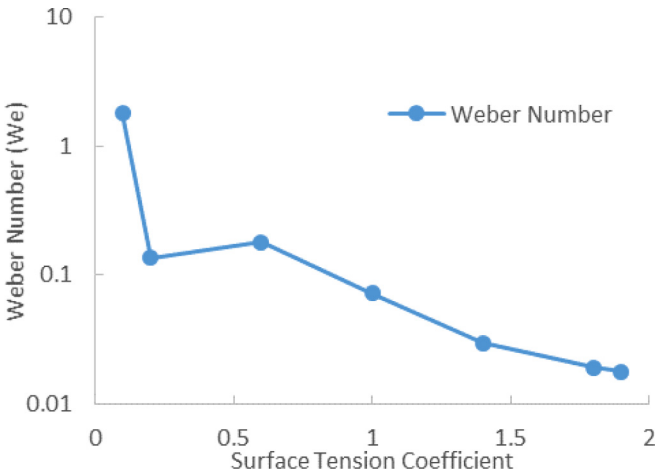

FIG. 12. Semi-log trend of the Weber number of the departing bubbles at different values of the surface tension coefficient.

$$\rho_2(T_r = 1.0 - 0.9) = -21441T^2 + 4162.8T - 196.16, \tag{43}$$

$$\rho_2(T_r = 0.9 - 0.8) = -2465T^2 + 341.82T - 3.8995, \tag{44}$$

$$\rho_2(T_r = 0.8 - 0.6) = -16225T^3 + 2771.6T^2 - 205.9T + 14.802. \tag{45}$$

Table IV compares the values of spinodal points obtained using the polynomial equations with the values calculated using the mechanical and chemical equilibrium equations.

Droplet evaporation simulations were carried out in order to compare the performance of our piecewise-linear thermal model with the YS and MPI thermal models. The parameters in the Peng-Robinson equation of state were set to $a = 3/49$, $b = 2/21$, $R = 1$, and the acentric parameter was equal to 0.344 (the acentric parameter value for water). MPI was implemented using the adapted Li-Luo forcing method with $\varepsilon_{\mathrm{Forcing},j}$ set to 0.89 times the value of $\varepsilon_{\mathrm{EOS},j}$. The YS method was implemented using the Huang-Wu forcing method with k_1 set to 0.0 and k_2 set to -0.2188. The piecewise-linear method

TABLE III. Spinodal points calculated at a number of reduced temperatures for the Peng-Robinson EOS with $a = 3/49$, $b = 2/21$, $R = 1$, and acentric factor equal to 0.344. In the piecewise-linear EOS, Θ_v was set to 0.213 33, θ_L to 0.333 33, and θ_M to -0.003 33.

T_r	T	ρ_1	ρ_2
1	0.109378	2.657309	2.657309
0.95	0.103909	1.03	4.9009
0.9	0.09844	0.59	5.861942
0.85	0.092972	0.35	6.572979
0.8	0.087503	0.204	7.136564
0.75	0.082034	0.114	7.60679
0.7	0.076565	0.059	8.002541
0.65	0.071096	0.0275	8.343035
0.6	0.065627	0.0111	8.640901

TABLE IV. Comparison of the spinodal points obtained from the polynomial equations with the spinodal points calculated using the mechanical and chemical equilibrium equations.

T_r	ρ_1 polynomial	ρ_1 polynomial/ ρ_1	ρ_2 polynomial	ρ_2 polynomial/ ρ_2
1	2.6637	1.0024	2.6482	0.9966
0.95	1.0359	1.0057	4.8921	0.9982
0.9	0.5894	0.9989	5.8623	1.0001
0.85	0.3494	0.9983	6.5733	1.0000
0.8	0.2036	0.9980	7.1369	1.0000
0.75	0.1139	0.9990	7.6058	0.9999
0.7	0.0585	0.9916	8.0025	1.0000
0.65	0.0275	1.0001	8.3421	0.9999
0.6	0.0109	0.9844	8.6404	0.9999

was implemented using the Huang-Wu forcing method with k_1 set to 0.0 and k_2 set to -0.2288 at a reduced temperature equal to 0.86. The value of k_2 parameter was changed to -0.15 for simulations with the thermal piecewise-linear method at a reduced temperature of 0.8. Figure 13 shows the evaporation rates for the different hybrid models at a reduced temperature equal to 0.86, and Fig. 14 illustrates the evaporation rates of the different DDF models at a reduced temperature set to 0.8. It is clear that the piecewise-linear models with temperature-dependent spinodal points produce the highest rates of evaporation. The evaporation lines obtained using the piecewise-linear models are also the least straight, which is a negative factor for the model.

2. *Envelope of stable reduced temperatures*

Now that a piecewise-linear thermal model has been presented, it is possible to investigate reduced temperature simulation capabilities of the three pseudopotential-based thermal models. First of all, in order to facilitate discussion of the temperature-lowering capabilities of the pseudopotential-based models, any differences between the hybrid and modified temperature DDF models should be highlighted. According to Table V, DDF models are more stable than hybrid models. The simulations were carried out as droplet evaporation cases with the superheat applied being greater than the liquid saturation temperature by 0.14 times the critical temperature (i.e., superheat $= T_{\text{sat}} + 0.14T_c$). Hence, it can be suggested that DDF models are more suitable for the investigation of the lowest achievable reduced temperatures.

Table VI compares the reduced temperature-lowering capabilities of the YS thermal DDF model, the MPI thermal DDF model, and the piecewise-linear thermal DDF model. Again, the simulations were carried out for droplet evaporation with the superheat greater than the saturation temperature

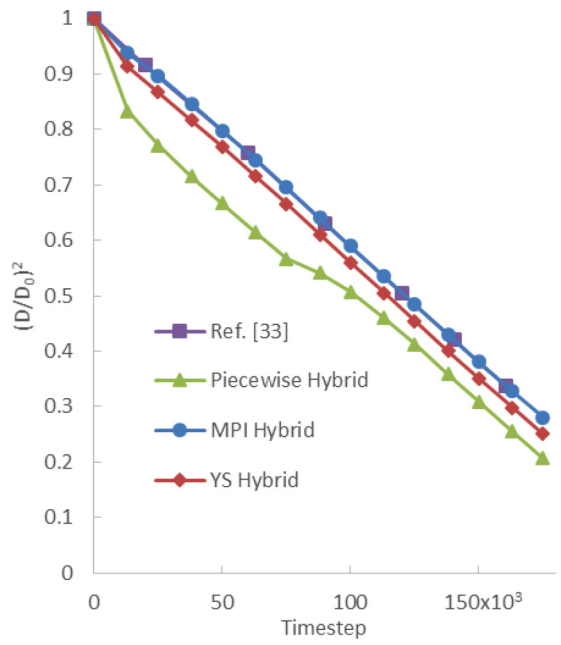

FIG. 13. Comparison of the evaporation rates of different models at a reduced temperature of 0.86. Reference [33] data included for comparison. D_0 was set to 60 lattice units.

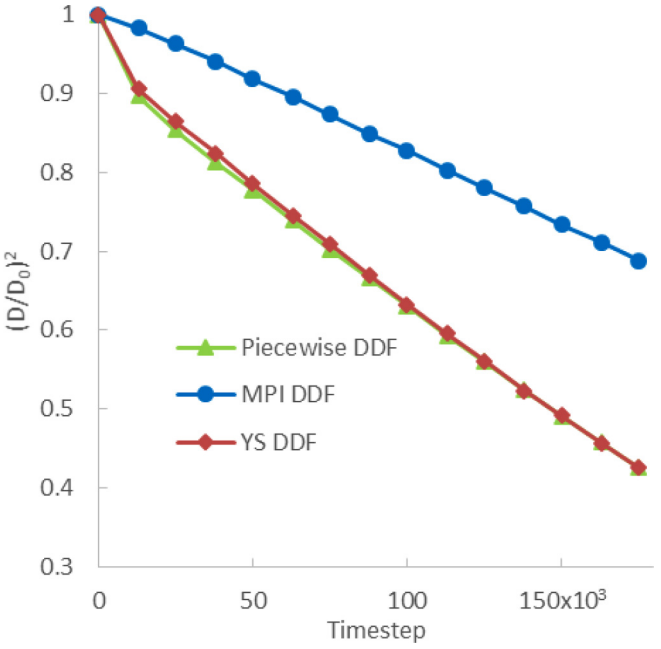

FIG. 14. Comparison of the evaporation rates of different models. The reduced temperature was equal to 0.8, and D_0 was equal to 60 lattice units.

TABLE V. Temperature reduction stability results obtained using hybrid and DDF models. Simulations were carried out using the Peng-Robinson EOS with $a = 3/49$, $b = 2/21$, $R = 1$, and acentric factor = 0.344.

T_r	YS thermal DDF	YS thermal hybrid	MPI thermal DDF	MPI thermal hybrid
0.86	Stable	Stable	Stable	Stable
0.8	Stable	Unstable	Stable	Unstable

TABLE VI. Temperature reduction stability results for the three different pseudopotential-based thermal models combined with DDF. Simulations were carried out using the Peng-Robinson EOS with $a = 3/49$, $b = 2/21$, $R = 1$, and acentric factor = 0.344.

Reduced temperature	YS thermal	MPI thermal	Piecewise thermal
0.86	Stable	Stable	Stable
0.8	Stable	Stable	Stable
0.78	Unstable	Stable	Unstable
0.76	Unstable	Unstable	Unstable

by $0.14T_c$. YS and piecewise-linear models achieved the same reduced temperature of 0.8, while the MPI thermal model was able to achieve a reduced temperature of 0.78. This suggests that MPI thermal models are more suitable for carrying out simulations whose purpose is to investigate thermal effects at low reduced temperatures.

Clearly, thermal models have problems in carrying out simulations at low reduced temperatures. The simulations discussed above were carried out using the Peng-Robinson equation of state with a set to $3/49$, b to $2/21$, R to 1, and the acentric factor set to the value for water, i.e., 0.344. The usual strategy for improving the stability of simulations is to increase interfacial thickness. In Fig. 15 , it can be observed that the simulation carried out at a reduced temperature of 0.78 with $a = 3/49$ and $b = 2/21$ is on the verge of the stable simulation envelope. The sign that the simulation is close to instability manifests itself in the fluctuations of droplet diameter around 13 000 and 50 000 time steps. Therefore, in order to improve stability and achieve lower reduced temperatures, an attempt can be made to increase the interfacial thickness. This can be achieved by lowering the value of the a parameter in the cubic EOS, as originally demonstrated by Li *et al.* [29]. However, this strategy offers only limited success in achieving lower reduced temperatures in thermal simulations. In Fig. 15 it can be seen that increasing interfacial thickness allows us to lower the achievable reduced temperature down to 0.76. To achieve even lower reduced temperatures, the b parameter in the cubic EOS also has to be decreased. Coexistence densities are not dependent on the a parameter in the Peng-Robinson and Carnahan-Starling equations of state. However, they are dependent on the b parameter, which means that the coexistence densities have to be recalculated each time the b parameter is adjusted. Adjusting the values of both parameters in the Peng-Robinson EOS allows us to achieve stable droplet evaporation simulations at $T_r = 0.6$. As depicted in Fig. 15, the rate of evaporation decreases at a constant superheat applied to the droplet, as the reduced temperature is lowered. Even as the superheat is increased, the rate of evaporation is not a straight line at high density ratios. In the early stages of evaporation simulations at $T_r = 0.6$, the droplet diameter even exceeds the initial diameter. This indicates that it is difficult to achieve good accuracy at lower reduced temperatures, even if the simulations are stable.

Figure 16 examines the effects of changing the a and b parameters in the Peng-Robinson equation of state on the

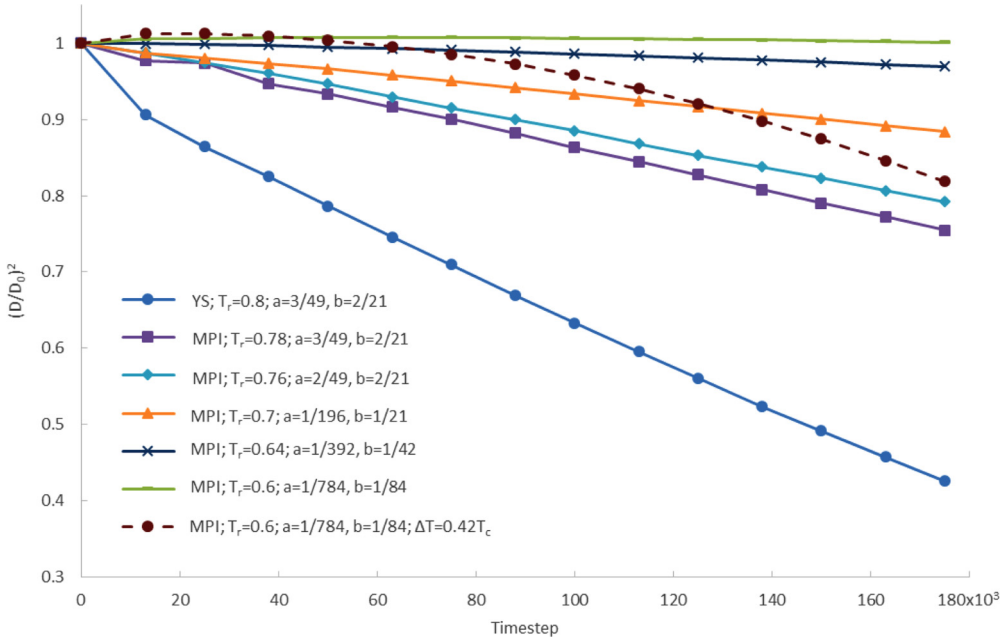

FIG. 15. Results of droplet evaporation simulations at a range of reduced temperatures. Simulations at lower reduced temperatures were made possible by lowering of the a and b parameters in the Peng-Robinson EOS. As in the previous cases, $D_0 = 60$.

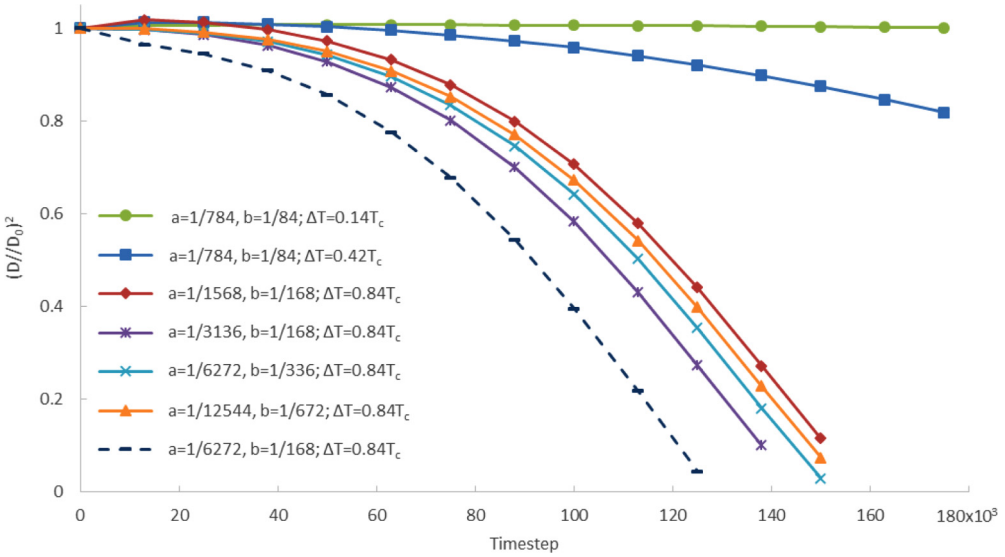

FIG. 16. Details of the effect of adjusting the Peng-Robinson EOS parameters on droplet evaporation at $T_r = 0.6$ with $D_0 = 60$.

rate of evaporation of a droplet when the thermal MPI DDF model is applied at $T_r = 0.6$. The main problem encountered involves the rate of evaporation not conforming to the D^2-law. Increasing interfacial thickness can have beneficial effects on the rate of evaporation. For example, at a constant value of b equal to 1/168, the rate of evaporation improved as a was decreased from 1/1568 to 1/3136 and then again as it was decreased further to 1/6272. The best results were achieved when a was equal to 1/6272 and b was equal to 1/168. Lowering the value of b to 1/336 while keeping a at 1/6272 did not improve the results obtained. Lowering both a and b parameters even further from those identified as optimal (i.e., from $a = 1/6272$, $b = 1/168$) again did not improve the rate of evaporation.

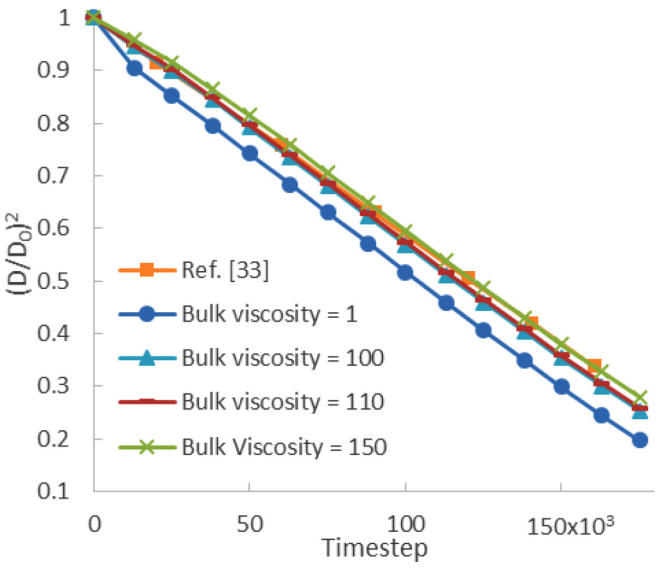

FIG. 17. The effect of increasing bulk viscosity as a multiple of kinematic viscosity on the rate of droplet evaporation. Comparison to data in Ref. [33]. The initial droplet diameter (D_0) was 60 lattice units.

F. Effects of MRT and forcing scheme parameters on droplet evaporation

In discussions of thermal models in the literature, some material parameters are not mentioned. For example, Li *et al.* [16] and Li *et al.* [33] employed the MRT collision operator with methods of adjusting thermodynamic consistency, but they did not mention the settings of the MRT relaxation rates or of the ε parameter for adjusting thermodynamic consistency in the forcing scheme. These parameters have an effect on the rate of evaporation and could affect the

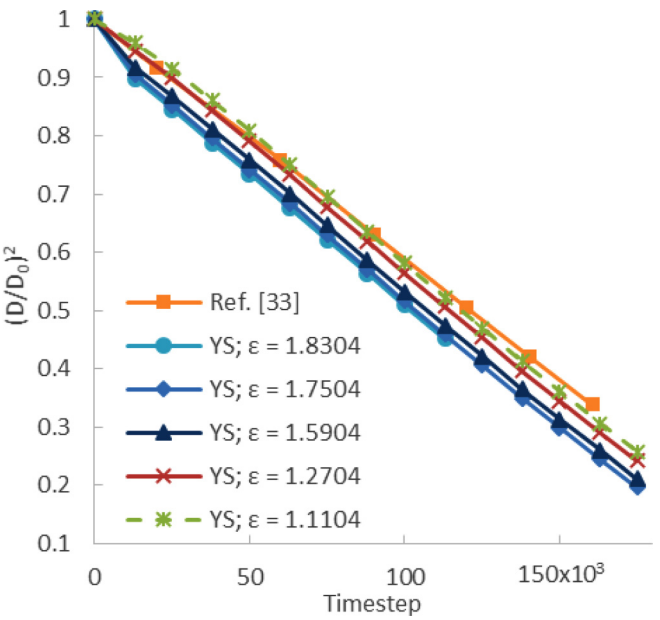

FIG. 18. The influence of modifying ε in the Huang-Wu scheme [36] for the adjustment of thermodynamic consistency. k_1 was set to 0 in order to avoid modifying surface tension, and k_2 was varied in order to change the value of ε. Evaporation rates are compared to data in Ref. [33] using the same initial droplet diameter of 60 lattice units.

slope and any deviation from linearity of the D^2 plots. They are briefly explored in Figs. 17 and 18. It can be seen in Fig. 17 that increasing the value of bulk viscosity decreases the rate of evaporation. Decreasing ε has an effect on the coexistence densities, and it slows down the reduction in the droplet's diameter, as depicted in Fig. 18. The effects of these parameters should be kept in mind when comparing different models.

V. CONCLUSIONS

The task set out in this work of developing MPI [3,4] into a simulation tool capable of thermal simulations was achieved. MPI's characteristics, which make it an interesting model, include an increased number of tuneable parameters compared to other pseudopotential models. The higher number of tuneable parameters can grant modelers greater control over simulations. MPI was combined with the MRT [27] collision operator using an adapted version of Li-Luo's [29] forcing scheme. A combination of multiphase models with collision operators more advanced than the BGK [28] collision operator is advisable for challenging applications. A method of approaching thermodynamic consistency using MPI was proposed here. Where required, MPI models can be tuned to approach thermodynamic consistency by splitting the ε_j parameter into two parts, i.e., $\varepsilon_{\mathrm{EOS},j}$ for use in enforcing the equation of state in the calculations of interparticle interactions, and $\varepsilon_{\mathrm{Forcing},j}$ for use in the forcing scheme adjustment of thermodynamic consistency.

The MPI interparticle force expression was modified from the isothermal expression to an expression that includes thermal effects at the local and neighboring sites and is suitable for thermal cases. The MPI model was successfully combined with Li *et.al.*'s DDF thermal model [16] and Li *et al.*'s hybrid thermal model [15]. MPI thermal models correctly simulate droplet evaporation and obey the D^2-law [18] well. The droplet evaporation rates obtained using MPI compare favorably compared to droplet evaporation rates produced using YS-based [30] or piecewise linear-based [25] pseudopotential thermal models. MPI was also combined with Huang-Wu's [36] and Li-Luo's [35] methods of surface tension adjustment. Surface tension was successfully modified in bubble nucleation simulations during nucleate pool boiling. Bubble shape varied from teardrop to dome or mushroom shapes.

It was also found in this work that MPI thermal models are comparatively better-suited to thermal simulations at low reduced temperatures. Thermal simulations at high density ratios are challenging for thermal models. Simulations of droplet evaporation were carried out at a reduced temperature of 0.6 by lowering the a and b parameters in the Peng-Robinson equation of state. The best results were obtained with $a = 1/6272$ and $b = 1/168$. During nucleate pool boiling simulations, bubble departure from the heating element has not been achieved at $T_r = 0.6$.

ACKNOWLEDGMENTS

This work has received funding from the European Union's Horizon 2020 research and innovation programme under Grant Agreement No. 654462 (STEMM-CCS) and the Research Council of Norway through the CLIMIT program funded project no. 254711 (Baymode). The first author gratefully acknowledges support from the Alexander Neilson scholarship.

[1] G. R. McNamara and G. Zanetti, Use of the Boltzmann Equation to Simulate Lattice-Gas Automata, Phys. Rev. Lett. **61**, 2332 (1988).

[2] Y. Koizumi, Outline of boiling phenomena and heat transfer characteristics, in *Boiling*, edited by Y. Koizumi, M. Shoji, M. Monde, Y. Takata, and N. Nagai (Elsevier, Boston, 2017), Chap. 1, pp.1–11.

[3] S. Khajepor, J. Wen, and B. Chen, Multipseudopotential interaction: A solution for thermodynamic inconsistency in pseudopotential lattice Boltzmann models, Phys. Rev. E **91**, 023301 (2015).

[4] S. Khajepor and B. Chen, Multipseudopotential interaction: A consistent study of cubic equations of state in lattice Boltzmann models, Phys. Rev. E **93**, 013303 (2016).

[5] X. Shan and H. Chen, Lattice Boltzmann model for simulating flows with multiple phases and components, Phys. Rev. E **47**, 1815 (1993).

[6] X. W. Shan and H. D. Chen, Simulation of nonideal gases and liquid-gas phase-transitions by the lattice Boltzmann-equation, Phys. Rev. E **49**, 2941 (1994).

[7] Q. Li, K. H. Luo, Q. J. Kang, Y. L. He, Q. Chen, and Q. Liu, Lattice Boltzmann methods for multiphase flow and phase-change heat transfer, Prog. Energy Combust. Sci. **52**, 62 (2016).

[8] F. Chen, A. Xu, G. Zhang, Y. Li, and S. Succi, Multiple-relaxation-time lattice Boltzmann approach to compressible flows with flexible specific-heat ratio and Prandtl number, Europhys. Lett. **90**, 54003 (2010).

[9] X. Shan, Simulation of Rayleigh-Bénard convection using a lattice Boltzmann method, Phys. Rev. E **55**, 2780 (1997).

[10] P. Lallemand and L.-S. Luo, Hybrid finite-difference thermal lattice Boltzmann equation, Int. J. Mod. Phys. B **17**, 41 (2003).

[11] X. He, S. Chen, and G. D. Doolen, A novel thermal model for the lattice Boltzmann method in incompressible limit, J. Comput. Phys. **146**, 282 (1998).

[12] Z. Guo, C. Zheng, B. Shi, and T. S. Zhao, Thermal lattice Boltzmann equation for low Mach number flows: Decoupling model, Phys. Rev. E **75**, 036704 (2007).

[13] O. Filippova and D. Hänel, A novel lattice BGK approach for low Mach number combustion, J. Comput. Phys. **158**, 139 (2000).

[14] S. V. Patankar, *Numerical Heat Transfer and Fluid Flow* 1st ed. (Hemisphere, 1980).

[15] Q. Li, Q. J. Kang, M. M. Francois, Y. L. He, and K. H. Luo, Lattice Boltzmann modeling of boiling heat transfer: The boiling curve and the effects of wettability, Int. J. Heat Mass Transf. **85**, 787 (2015).

[16] Q. Li, P. Zhou, and H. J. Yan, Improved thermal lattice Boltzmann model for simulation of liquid-vapor phase change, Phys. Rev. E **96**, 063303 (2017).
[17] S. Gong and P. Cheng, A lattice Boltzmann method for simulation of liquid-vapor phase-change heat transfer, Int. J. Heat Mass Transf. **55**, 4923 (2012).
[18] C. K. Law, Recent advances in droplet vaporization and combustion, Prog. Energy Combust. Sci. **8**, 171 (1982).
[19] Q. Li, J. Y. Huang, and Q. J. Kang, On the temperature equation in a phase change pseudopotential lattice Boltzmann model, Int. J. Heat Mass Transf. **127**, 1112 (2018).
[20] W. Gong, Y. Y. Yan, S. Chen, and E. Wright, A modified phase change pseudopotential lattice Boltzmann model, Int. J. Heat Mass Transf. **125**, 323 (2018).
[21] A. Hu, R. Uddin, and D. Liu, Discrete methods of the energy equations in the pseudo-potential lattice Boltzmann model based simulations, Comput. Fluids **179**, 645 (2019).
[22] G. Hazi and A. Markus, On the bubble departure diameter and release frequency based on numerical simulation results, Int. J. Heat Mass Transf. **52**, 1472 (2009).
[23] Y. Peng, C. Shu, and Y. Chew, Simplified thermal lattice Boltzmann model for incompressible thermal flows, Phys. Rev. E **68**, 026701 (2003).
[24] R. Zhang and H. Chen, Lattice Boltzmann method for simulations of liquid-vapor thermal flows, Phys. Rev. E **67**, 066711 (2003).
[25] C. E. Colosqui, G. Falcucci, S. Ubertini, and S. Succi, Mesoscopic simulation of non-ideal fluids with self-tuning of the equation of state, Soft Matter **8**, 3798 (2012).
[26] A. Hu and D. Liu, A superheat degree driven liquid-vapor phase-change lattice Boltzmann model, Int. J. Heat Mass Transf. **136**, 674 (2019).
[27] D. d'Humieres, *Generalized Lattice-Boltzmann Equations in Rarefied Gas Dynamics: Theory and Simulations*, Vol. 159 (Progress in Astronautics and Aeronautics: AIAA, 1994), p. 450.
[28] P. L. Bhatnagar, E. P. Gross, and M. Krook, A model for collision processes in gases. I. Small amplitude processes in charged and neutral one-component systems, Phys. Rev. **94**, 511 (1954).
[29] Q. Li, K. H. Luo, X. J. Luo, and X. J. Li, Lattice Boltzmann modeling of multiphase flows at large density ratio with an improved pseudopotential model, Phys. Rev. E **87**, 053301 (2013).
[30] P. Yuan and L. Schaefer, Equations of state in a lattice Boltzmann model, Phys. Fluids **18**, 042101 (2006).
[31] T. Lee and C.-L. Lin, A stable discretization of the lattice Boltzmann equation for simulation of incompressible two-phase flows at high density ratio, J. Comput. Phys. **206**, 16 (2005).
[32] S. P. Thampi, S. Ansumali, R. Adhikari, and S. Succi, Isotropic discrete Laplacian operators from lattice hydrodynamics, J. Comput. Phys. **234**, 1 (2013).
[33] Q. Li, Q. J. Kang, M. M. Francois, and A. J. Hu, Lattice Boltzmann modeling of self-propelled Leidenfrost droplets on ratchet surfaces, Soft Matter **12**, 302 (2015).
[34] L. Chen, Q. Kang, Y. Mu, Y.-L. He, and W.-Q. Tao, A critical review of the pseudopotential multiphase lattice Boltzmann model: methods and applications, Int. J. Heat Mass Transf. **76**, 210 (2014).
[35] Q. Li and Q. Luo, Achieving tunable surface tension in the pseudopotential lattice Boltzmann modeling of multiphase flows, Phys. Rev. E **88**, 053307 (2013).
[36] R. Huang and H. Wu, Third-order analysis of pseudopotential lattice Boltzmann model for multiphase flow, J. Comput. Phys. **327**, 121 (2016).
[37] C. Pozrikidis, *Fluid Dynamics Theory, Computation, and Numerical Simulation*, 2nd ed. (Springer, Boston, 2009).
[38] B. E. Rapp, Fluids, in *Microfluidics: Modelling, Mechanics and Mathematics*, edited by B. E. Rapp (Elsevier, Oxford, 2017), Chap. 9, pp.243–263.
[39] P. K. Unnikrishnan, V. Vaikuntanathan, and D. Sivakumar, Impact dynamics of high weber number drops on chemically modified metallic surfaces, Colloids Surf. A **459**, 109 (2014).
[40] A. Montessori, P. Prestininzi, M. La Rocca, and S. Succi, Entropic lattice pseudo-potentials for multiphase flow simulations at high weber and reynolds numbers, Phys. Fluids **29**, 092103 (2017).
[41] N. I. Kolev, *Multiphase Flow Dynamics 2: Mechanical Interactions*, 4th ed. (Springer, Berlin, 2011).
[42] J. Campbell, Entrainment, in *Complete Casting Handbook*, 2nd ed., edited by J. Campbell (Butterworth-Heinemann, Boston, 2015), Chap. 2, pp.17–90.